

Satellite-based estimates of high-resolution CO concentrations at ground level in the Yangtze River Economic Belt of China

Jiaqi Dong ^a, Xiuying Zhang ^{a,b,c,*}, Nan Zhan ^{a,c}

^a International Institute for Earth System Science, Nanjing University, Nanjing, 210046, China

^b Jiangsu Center for Collaborative Innovation in Geographical Information Resource Development and Application, Nanjing, 210023, China

^c Key Laboratory of Urban Land Resources Monitoring and Simulation, Ministry of Natural Resources, Shenzhen, 518000, China



HIGHLIGHTS

- Ground-level CO concentrations with the spatial resolution of $0.25^\circ \times 0.25^\circ$ are inferred from MOPITT CO columns and CAM-CHEM.
- Ground-level CO concentrations are downscaled to $1 \times 1 \text{ km}^2$ based on an algorithm of MGWR model with the auxiliary factors.
- Hotspots of CO concentrations are concentrated in the northern Yangtze River Delta and the urban areas.
- High CO values occur in winter, while low in summer.

ARTICLE INFO

Keywords:

Ground-level CO concentrations
Satellite CO columns
Chemical transport model
MGWR model
Yangtze River Economic Belt of China

ABSTRACT

This study proposed a method to downscale ground-level CO concentrations from satellite observations. Taking the Yangtze River Economic Belt of China as the study area, ground-level CO concentrations ($0.25^\circ \times 0.25^\circ$) were first estimated from the troposphere (MOPITT) CO columns and atmospheric CO profiles simulated by the chemical transport model CAM-CHEM; then the resulting data was downscaled to $1 \times 1 \text{ km}^2$ based on an algorithm of multiscale geo-weighted regression (MGWR) model with the auxiliary factors. The estimated ground-level CO concentrations were in good agreement with the observations at ground-based sites (RMSE = 0.25 mg/m³, PRE = 19%). In the Yangtze River Economic Belt, monthly ground-level CO concentrations showed obvious temporal and spatial variations, ranging from 0.30 to 0.81 mg/m³ and an average of 0.49 mg/m³; high CO values occurred in winter, while low in summer; hotspots of CO concentrations were concentrated in the northern Yangtze River Delta and the urban areas.

1. Introduction

Carbon monoxide (CO) is the most carbon-containing component in the atmosphere, other than carbon dioxide (CO₂) and methane (CH₄) (Ma et al., 2021). CO exists for about three months in atmosphere and is commonly used as a tracer of global atmospheric pollution and transmission (Liu et al., 2019). CO emissions from local areas can diffuse widely into the troposphere and middle atmosphere through vertical and horizontal transport in the atmospheric circulation, which is more pronounced at mid-latitude regions (Allen et al., 1999). The emitted CO can affect the composition of the atmospheric environment by influencing the levels of hydroxide (OH⁻) and other important trace gases such as CO₂, Ozone (O₃), and CH₄ (Zhang and Wang, 2001). Therefore, it is necessary to gain accurate CO emissions on a regional scale. However,

it is not easy to obtain gridded CO emissions, nevertheless they can be represented by ground-level CO concentrations.

The national monitoring network for CO concentrations in China has a high temporal resolution, however it has poor mobility and spatial coverage (Xu et al., 2014). Another method to determine the gridded CO concentrations is a chemical transport model (CTM). A CTM uses meteorological parameters created by meteorological models as input conditions to simulate the reaction, transmission, and deposition of pollutants in the atmosphere. However, CO concentrations were often underestimated, mainly because the emission inventory cannot cover all anthropogenic CO emissions, such as biomass combustion, residential biofuel consumption, and emissions from transient fire events (Wang et al., 2002; Hu et al., 2016).

Compared with the ground-based measurements and CTM, satellite

* Corresponding author. International Institute for Earth System Science, Nanjing University, Nanjing, 210046, China.

E-mail address: zhangxy@nju.edu.cn (X. Zhang).

remote sensing could monitor CO concentrations at a global coverage on a continuous and repeatable basis to monitor atmospheric CO. The sensors include the Atmospheric Infrared Sounder (AIRS), the Measurements of Pollution in the Troposphere (MOPITT), the TROPOspheric Monitoring Instrument (TROPOMI), the Scanning Imaging Absorption SpectroMeter for Atmospheric CHartographY (SCIAMACHY), etc (Smith et al., 1999). These satellite-based measurements on CO columns have been used to describe the spatial and temporal variability of atmospheric CO, to assess the level of atmospheric pollutants in a region, to determine the effectiveness of emission policies, and as input data for statistical models (Cen et al., 2015; Zheng et al., 2018; Liu et al., 2019).

Although satellite observations on CO columns have been widely used as a proxy for spatially varying ground-level concentrations in the atmosphere, there is a large difference between CO columns and the ground-level CO concentrations, due to the variability of the vertical profile of CO in the atmosphere. Related studies have shown that gaseous pollutants emitted disperse vertically and horizontally and show a certain gradient in vertical space from the ground to high altitude (Kollonige et al., 2018). The differential absorption spectroscopy technique is widely used in atmospheric environmental monitoring, which has been used to observe the vertical profiles of a variety of atmospheric pollutants (Wang et al., 2006; Hu et al., 2019). Atmospheric pollutant concentrations at different altitudes can also be measured directly in the air using delivery vehicles such as balloons and airplanes (Glaser et al., 2003; Chen et al., 2012). However, differential absorption spectroscopy has a large error in low contaminant gas columns (Yan et al., 2017) and the vertical distribution information contained in direct measurements has limitation that cannot allow detailed inversion of contaminant gas profiles over a large area. Therefore, we developed a method to calculate atmospheric CO profiles. CTMs were used to simulate CO profiles for each pixel cell, and the ground-level CO concentrations were estimated by combining the CO columns with the CTM-simulated atmospheric CO profiles. A series of ground-level pollutant concentrations have been obtained by applying CTM-assisted satellite observations (Lamsal et al., 2008; Gu et al., 2017; Zhang et al., 2017). These studies have shown that the use of CTM-assisted satellite observations for estimating ground-level pollutants is feasible.

The CO columns provided by a single sensor usually have the low spatial resolution. Resolving spatial heterogeneity by building statistical regressions is used to improve the degree of geographical information refinement representation (Goodchild, 2013). Statistical regressions of downscaling method are based on the assumption of “constant relational scale” (Zhu et al., 2021), applying spatial relationships at low spatial resolution to high spatial resolution and increasing spatial texture information based on high-resolution auxiliary parameters. It has been widely used to improve the spatial resolution of data from satellite images and quantitative remote sensing products such as temperature (Wang et al., 2021), precipitation (Li and Zhang, 2015), and soil moisture (Wei et al., 2019). Among statistical downscaling methods, the geographically weighted regression statistical models (GWR) are based on local weighted regression theory, which has been widely used in the estimation of pollutant distribution at small scales (Lu et al., 2014; Alahmadi et al., 2019; Zhang et al., 2020). Given that the range of scale factors will have different degrees of influence on the results of regression models, considering the spatially heterogeneous scale effects of each influencing factor in the process in downscaling CO concentrations will likely enhance the accuracy of downscaling. Fotheringham et al. (2017) proposed a multiscale geo-weighted regression model (MGWR) to process downscaling, which has loosened the assumptions on the same spatial scale in the modeling process based on GWR. In this paper, we selected the Yangtze River Economic Belt as the study area, and proposed a spatial downscaling method for CO products based on the MGWR model to obtain high-spatial-resolution CO concentration data, and then evaluated the results.

This study attempted to obtain the gridded ground-level CO concentration with a high-spatial resolution, derived by MOPITT CO

column and CTM-simulated atmospheric CO profiles, based on a MGWR model. First, monthly ground-level CO concentrations were inferred using MOPITT CO columns and atmospheric CO profiles simulated by CAM-CHEM. Then, available fine spatial resolution auxiliary data were selected and the algorithm based on the MGWR model was used to improve the spatial resolution of ground-level CO concentrations to $1\text{ km} \times 1\text{ km}$, and the spatial distribution pattern of the regression coefficients for the factors was discussed. Finally, the spatial and temporal variations of ground-level CO concentrations in the Yangtze River Economic Belt were analyzed.

2. Study area, materials, and methods

2.1. Study area

This study evaluated ground-level CO concentration across the Yangtze River Economic Belt in 2020. The Yangtze River Economic Belt is the longest and most extensive economic belt in China, accounting for 43% of the population and 46.4% of the national GDP in 2021. However, the expansion of the economy activities has led to problems such as air and environmental pollution. Carbon emissions in the Yangtze River Economic Belt have reached 330.8 Mt in 2019, accounting for 45.2% of the national total (Liu et al., 2018). In addition, the industrial structure, quantity of resources, technology level and economic activities vary greatly between provinces and cities, which contributes to the uneven spatially-distributed pattern of CO emissions (Yang et al., 2022). Therefore, it is of great theoretical and practical significance to grasp the current situation of ground-level CO concentrations in the 11 provinces along the Yangtze River Economic Belt and analyze the influencing factors.

2.2. Materials used in this study

2.2.1. Atmospheric CO vertical columns from MOPITT

The MOPITT sensor on board the Terra satellite is a multi-channel radiometric instrument that detects atmospheric CO concentrations in the $4.7\text{ }\mu\text{m}$ band (thermal infrared channel) and the $2.3\text{ }\mu\text{m}$ band (near infrared channel). The satellite observations of CO tropospheric columns used in this study were obtained from the Atmospheric Science Data Center (<https://asdc.larc.nasa.gov/data/MOPITT/MOP2J.008/>). The MOPITT CO column has a horizontal extent of $22\text{ km} \times 22\text{ km}$. The files were originally formatted as HDF5 and converted by processing to Geotiff format with a spatial resolution of $0.25^\circ \times 0.25^\circ$. In this study, the CO columns from January 1, 2020 to December 31, 2020 were used. Negative CO columns were removed from the daily products, which were then combined into a dataset within one month. An inverse distance weighting (IDW) method was used to estimate the CO values at the gaps.

2.2.2. Atmospheric CO concentrations from CAM-CHEM

The Community Atmosphere Model with Chemistry (CAM-CHEM) was used to simulate the profile of CO concentrations (<https://www.acm.ucar.edu/cam-chem>). CAM-CHEM is designed to simulate tropospheric chemical and transport processes. The meteorologically driven data entered into the CAM-CHEM model were derived from MERRA-2 global reanalysis data developed by the Global Modeling and Assimilation Office at Goddard Space Flight Center. The anthropogenic emissions data that were input into the model were taken from sp5-85, while biogenic emissions were obtained from the online megan2.1 and fire emissions data were obtained from the $\text{CO}_2 \times$ fire inventory from National Center for Atmospheric Research emission ratio of the Fast Fire Emissions Dataset. The simulated CO concentrations have a $1.9^\circ \times 2.5^\circ$ horizontal resolution and 56 levels in altitude, temporally varying by 6 h every day. The data was integrated into a dataset within one month and each raster with $1.9^\circ \times 2.5^\circ$ was assigned to the CO columns according to the principle of closest proximity. And then, these data were used to

calculate the monthly averages of CO profiles in the atmosphere.

2.2.3. Ground measurements on CO concentrations

The in-situ measurements of hourly CO concentrations were used for accuracy assessment, which was obtained from the China National Environmental Monitoring Center (<http://www.cnemc.cn/>). These data were measured and recorded according to the Chinese Environmental Protection Standards HJ 193–2013 and HJ 655–2013. The dataset for the whole China region includes 1546 sites and there are 547 ground monitoring stations in the Yangtze River Economic Belt. The daily observations were pre-processed into a monthly average dataset. To match the satellite transit times, station monitoring data from 11:00–12:00 and 22:00–23:00 BST were selected. All available station monitoring data for the Yangtze River Economic Belt were used to assess the accuracy of ground-level CO concentrations.

2.2.4. Auxiliary data for spatial downscaling

Monthly temperature and precipitation data with the spatial resolution of 1 km × 1 km were obtained from the National Tibetan Plateau Science Data Center (<https://data.tpdc.ac.cn/>). This dataset integrates the global climate dataset published by Climatic Research Unit with the global high-resolution climate dataset published by WorldClim. The datasets were generated using the Delta spatial downscaling scheme and the validation by 496 independent meteorological observation sites showed that the dataset had good applicability in the Chinese region (Peng et al., 2019).

The NPP-VIIRS global nighttime lighting data was from NASA (<http://www.nasa.gov/NPP>). The Suomi National Polar-orbiting Partnership (SNPP) Visible Infrared Imaging Radiometer Suite (VIIRS) supports a Day-Night Band (DNB) sensor that provides global daily measurements of nocturnal visible and near-infrared (NIR) light that are suitable for earth system science and applications. The distribution of nighttime lights has a very close relationship with human activities, which has been widely used in urbanization studies, estimation of socio-economic indicators, and assessment in the field of ecology and environment (Cheng et al., 2017; Zheng et al., 2020; Hu et al., 2021).

The gridded population of the global dataset was from the NASA Socioeconomic Data and Applications Center (<https://sedac.ciesin.columbia.edu/data/set>). The dataset assigned populations to cells using the basic census and the proportional population assignment of administrative units. The data files were produced with a spatial resolution of 30 arc seconds.

The digital topographic elevation data was from the Shuttle Radar Topography Mission (<https://earthexplorer.usgs.gov/>). The dataset was generated by radar interferometry, an on-board/outboard antenna system, and a single data acquisition. Raw SRTM elevation data was processed by NASA Jet Propulsion Laboratory (JPL) c-band radar signals at 1 arc second intervals, while raw data from outside the United States is publicly released at 3 arc second intervals.

The land use data was obtained from the Data Center of the Institute of Geographical Sciences and Resources, Chinese Academy of Sciences (<http://www.resdc.cn/>). The national land use types were identified based on Landsat TM imagery from the United States and was generated through manual visual interpretation. The land use types include six primary types: farmland, woodland, grassland, water, residential land, and unused land.

2.3. Estimation of the ground-level CO concentrations and evaluation

The ground-level CO concentrations (C_{G_CO}) were estimated following the method to estimate the NO₂ concentrations from remotely sensed NO₂ columns (Lamsal et al., 2008; Zhang et al., 2017). A 2-dimensional to 6-dimensional Gaussian model was used to fit the CAM-CHEM-derived CO stratification concentrations in the vertical direction of the atmosphere on each raster. The basic form of the Gaussian model is expressed as Eq. (1). The vertical and crosswind dispersion of

atmospheric pollutants is assumed as Gaussian distribution, which could be traced back to 1947 (Sutton, 1947; Sørensen, 1998).

$$\rho(Z) = \sum_{i=2}^n \rho_{max,i} \exp\left(\frac{-(Z - Z_{0,i})^2}{\sigma_i^2}\right) \quad (1)$$

where $\rho(Z)$ is the model-indicated CO concentration at an atmospheric height of Z , $\rho_{max,i}$ refers to the maximum concentration along the vertical, $Z_{0,i}$ is the height at which the gaseous pollutant reaches its maximum concentration, and σ_i refers to the thickness of the buildup layer. To improve the accuracy of the fit, the model with the lowest root mean square error (RMSE) and the highest R² was used to estimate CO concentration along the atmospheric altitudes. For each selected raster image element, Eq. (2) was used to obtain the tropospheric columns for CAM-CHEM integrating from 0 to tropospheric height.

$$\Phi(Z_{trop}) = \int_0^{Z_{trop}} \rho(Z) \quad (2)$$

where Z_{trop} indicates the height of the top of the troposphere. Ground-level CO concentrations were estimated by combining satellite observations with concentrations simulated by CAM-CHEM (Eq. (3)).

$$C_{G_CO} = \frac{\rho(h)}{\Phi(Z_{trop})} \times C_{trop} \quad (3)$$

where $\rho(h)$ is the CO concentration at height h modelled by Eq. (1). In this study, the value of h is 20, which means that the CO concentrations at 20 m are selected as the ground level for CO concentrations. $\Phi(Z_{trop})$ denotes the tropospheric CO column modelled by CAM-CHEM in Eq. (2), and C_{trop} is the tropospheric CO column observed by satellite.

2.4. MGWR-based ground-level CO concentration downscaling algorithm

The MGWR package for the Python environment was used to downscale CO concentrations (Oshan et al., 2019). To accommodate the limitations of insufficient information at higher spatial resolutions, the spatial downscaling method needs to be accomplished by introducing additional information (Wang et al., 2014). In this study, high-resolution temperature (TMP), precipitation (PRE), topography (DEM), nighttime lighting (NTL), and population (POP) data mentioned in section 2.2.4 were selected as auxiliary covariates. Auxiliary data with a spatial resolution of 1 km × 1 km were resampled to a spatial resolution of 0.25° × 0.25°. The MGWR model was used to construct spatial relationships between CO concentrations (CO_{LR}) and auxiliary data ($DEM_{LR}, PRE_{LR}, TMP_{LR}, NTL_{LR}, POP_{LR}, LON_{LR}, LAT_{LR}$) with a spatial resolution of 0.25° × 0.25° as Eq. (4).

$$CO_{LR} = f(DEM_{LR}, PRE_{LR}, TMP_{LR}, NTL_{LR}, POP_{LR}, LON_{LR}, LAT_{LR}) + \varepsilon_{LR} \quad (4)$$

$f(*)$ denoted the best-fit functional relationship, which was constructed by Eq. (5).

$$y_i = \sum_{j=1}^k \beta_{bwj}(u_i, v_i)x_{ij} \quad (5)$$

where (u_i, v_i) represents the spatial geographic location of the point, y_i is the concentration of ground-level CO; x_{ij} is the value of the auxiliary variables; and β_{bwj} represents the jth local regression coefficient with bandwidth bw . Bandwidth bw is obtained by continuous experiments, and a bandwidth is selected in each experiment to fit the MGWR model and calculate Akaike Information Criterion (AIC), where AIC is defined as Eq. (6):

$$AIC = 2n \ln(\hat{\sigma}) + n \ln(2\pi) + n \frac{n + tr(S)}{n - 2 - tr(S)} \quad (6)$$

where $\hat{\sigma}$ is the predicted standard deviation of the error term and $tr(S)$ is

the trace of the hat matrix S . The bandwidth that minimizes the AIC is the chosen optimal bandwidth. Subject to spatial heterogeneity, the conversion process from coarse spatial resolution to high spatial resolution is affected by uncertainty, which is represented by the residuals (ε_{LR}).

$$\varepsilon_{LR} = CO_{LR} - G_S \quad (7)$$

where G_S is the CO concentration estimated by the MGWR model, ε_{LR} is the output resolution residual with a spatial resolution of $0.25^\circ \times 0.25^\circ$. Using IDW interpolation to interpolate to the spatial resolution of $1 \text{ km} \times 1 \text{ km}$, the high-resolution residual (ε_{HR}) is obtained.

$$CO_{HR} = f(DEM_{HR}, PRE_{HR}, TMP_{HR}, NTL_{HR}, POP_{HR}, LON_{HR}, LAT_{HR}) + \varepsilon_{HR} \quad (8)$$

The functional relationship $f(*)$ in Eq. (4) was applied to the CO concentration with auxiliary data with high spatial resolution (DEM_{HR} ; PRE_{HR} ; TMP_{HR} ; POP_{HR} ; NTL_{HR}) to obtain the spatial distribution of the CO concentrations with the spatial resolution of $1 \text{ km} \times 1 \text{ km}$ (CO_{HR}).

3. Results and discussion

3.1. Estimates of ground-level CO concentrations and accuracy assessment

When simulating atmospheric profiles of CO concentrations from CAM-CHEM with a 2–6 term Gaussian model, the R^2 of most raster fits could reach 0.99 (see Table A1 in SI.A), indicating the selected Gaussian model performed well in fitting the CO variations along the atmospheric heights. The fitted Gaussian model was then used to calculate CO columns and the ratio of ground-level CO concentrations to the total CO column. The ratios ranged from 0.003 to 0.044, presenting strong spatial variations. This ratio was then used to convert the CO columns to the ground-level concentrations, with a spatial resolution of $0.25^\circ \times 0.25^\circ$.

Considering the influencing factors on the spatial and temporal variations of the ground-level CO concentrations, NTL, POP, DEM, PRE, TMP combined with latitude and longitude were used to downscale the CO concentrations from $0.25^\circ \times 0.25^\circ$ to $1 \text{ km} \times 1 \text{ km}$. NTL and POP indicate the influence from human activities, DEM, latitude, and longitude represent the geographical influences, PRE and TMP are meteorological influencing factors. The globally adjusted R^2 of the MGWR model constructed for auxiliary variables and ground-level CO concentrations was 0.99, where 89% of the local R^2 was higher than 0.5 (see Fig.B1 in SI.B).

Monthly CO concentrations from 547 ground-based monitoring stations in the Yangtze River Economic Belt were used to evaluate the accuracy of the estimated ground-level CO concentrations with the spatial resolution of $0.25^\circ \times 0.25^\circ$ and $1 \text{ km} \times 1 \text{ km}$. The CO concentrations from individual stations corresponded to the pixel where they were located. The relative error of the observing values at each ground station against the simulated extracted values are shown in Fig. 2 (a) and (c). Fig. 2 (b) shows that approximately 58.3% of the sites had relative errors values between -30% and 30% for the CO concentrations with the spatial resolution of $0.25^\circ \times 0.25^\circ$, and the percentage of validation data with relative errors below -30% was 25%, indicating that the coarse resolution data cannot express the areas of high CO concentrations in

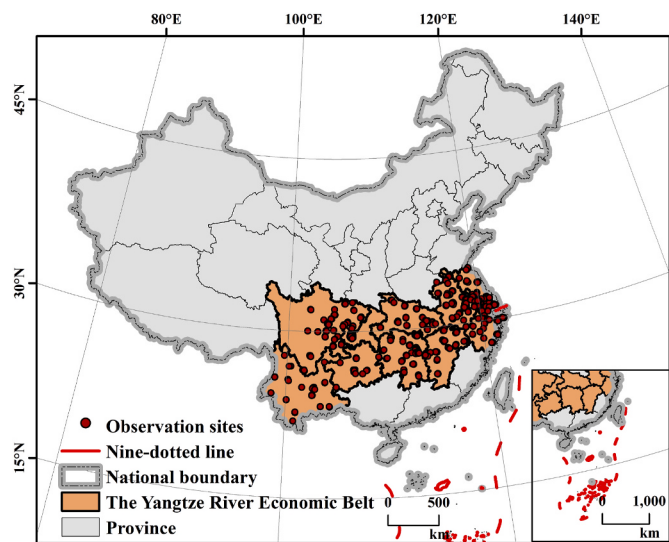


Fig. 1. Location of the Yangtze River Economic Belt in China, and sites of ground observations on CO concentrations.

western cities, where relative errors were all below -30% in provinces such as Yunnan and Guizhou.

For the data with a spatial resolution of $1 \text{ km} \times 1 \text{ km}$, the ratio of relative errors values within $-30\%-30\%$ increased to 76.5%. In addition, there was a significant reduction in the number of low value points of relative error in the western cities, with the percentage of data below -30% decreasing to 7%. These results indicated that the MGWR approach gained reliable downscaling results on ground-level CO concentrations. Fig. 2 (c) showed that the locations with high relative errors were mainly in the urban areas in the eastern region. Due to the high population concentration and the frequent human and industrial production activities, there was a tendency for the MGWR model to simulate higher CO concentrations than the ground observations. As a result, there was a high prediction error in the eastern urban areas, while in other areas the estimated results were in good agreement with the ground measurement results.

3.2. Spatial distribution of ground-level CO concentrations over the Yangtze River Economic Belt

The spatial distribution of the ground-level CO concentrations in 2020 and the regression coefficients for auxiliary variables estimated by the MGWR are shown in Fig. 3. The largest hotspot of CO concentrations in the Yangtze River Economic Belt is in the northern Yangtze River Delta region, with the most significant CO pollution in Jiangsu Province, Shanghai, northern Anhui Province and northern Zhejiang Province. The annual average of 1.14 mg/m^3 in the Yangtze River Delta is 133% higher than the average annual value of 0.49 mg/m^3 for the Yangtze River Economic Belt. CO concentrations gradually increased from the inland toward the coastline, which was consistent with the study by Yang et al. (2011). Coastal areas are densely populated and industrially developed, where anthropogenic emissions are high. The MIX inventory of anthropogenic CO emissions from sources developed by the Model Comparison Initiative for East Asia III and the United Nations Hemispheric Air Pollution Transport Program provided an inventory of anthropogenic CO emissions from four sectors: power, industry, residential, and transport (Li et al., 2017). The average value of anthropogenic CO emissions in the Yangtze River Economic Belt was 6.84 g/month/m^2 , with the emissions of the four CO sectors in the Yangtze River Delta region being $11.59 \text{ g/month/m}^2$, 69% higher than the average value of the whole region.

The hotspot in the Yangtze River Delta extended westward to form an

Table 1
The regression coefficients statistic of MGWR simulation.

Variable	Bandwidth	β_{\max}	β_{\min}	β_{ave}
Intercept	44	1.14	-1.08	0.03
TMP	44	0.95	-0.93	-0.31
PRE	44	0.57	-0.49	0.13
POP	193	3.8	0	1.21
NTL	1823	0.02	-0.01	0
DEM	44	0.08	-1.71	-0.30

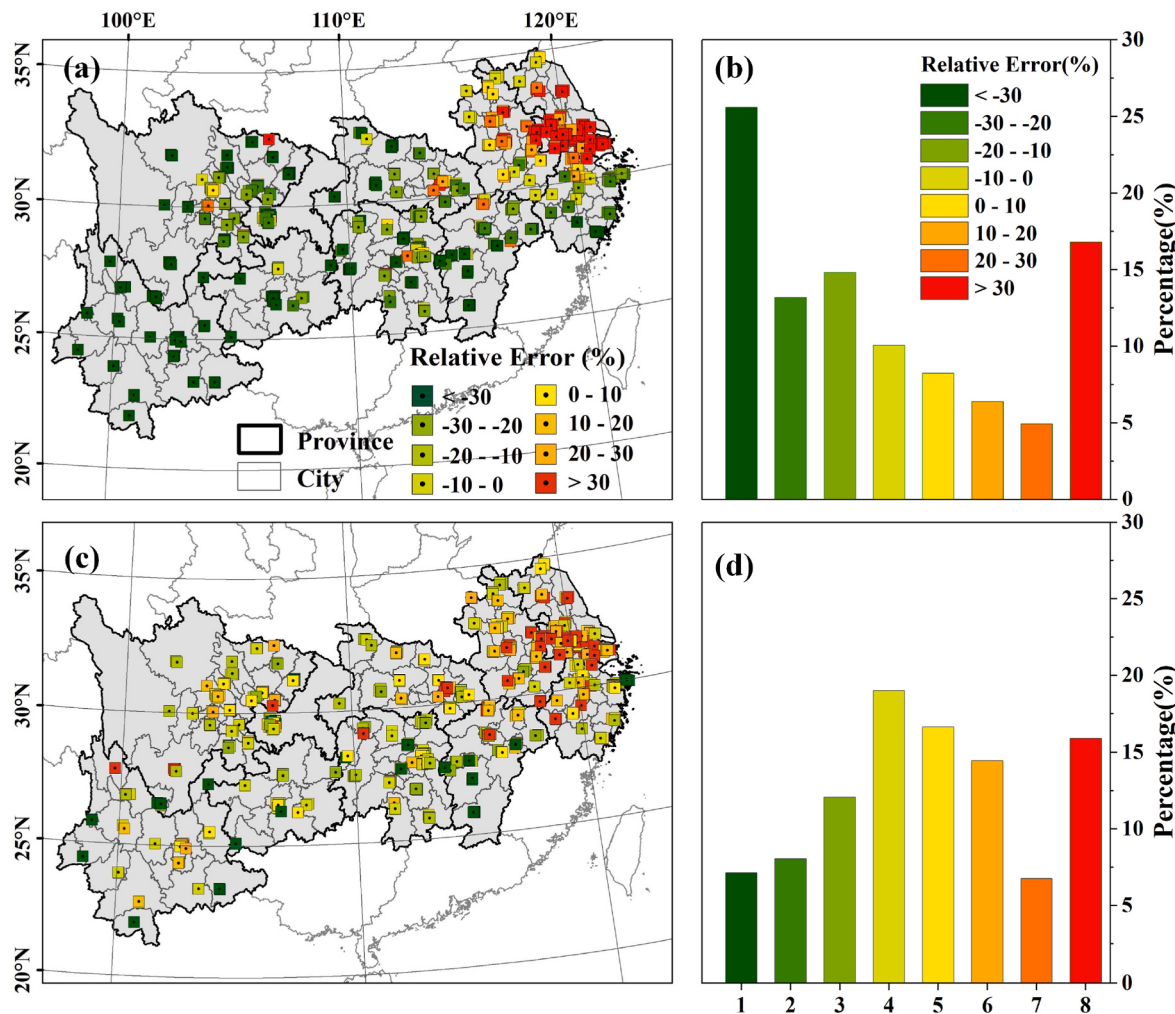


Fig. 2. Accuracy assessment (a)Relative error for CO concentrations with the spatial resolution of $0.25^\circ \times 0.25^\circ$ (b)Frequency distribution of relative error for CO concentrations with spatial resolution of $0.25^\circ \times 0.25^\circ$ (1–8 corresponds to the relative error < -30%, -30% to -20%, -20% to -10%, -10% - 0, 0–10%, 10%–20%, 20%–30%, >30%) (c) Relative error of CO concentrations with spatial resolution of $1\text{ km} \times 1\text{ km}$ (d)Frequency distribution of relative error for CO concentrations with spatial resolution of $1\text{ km} \times 1\text{ km}$.

area of high CO concentration aggregation in the eastern part of Hubei Province, centered on Wuhan, Yueyang and Yiyang in northern Hunan Province. Among them, the Jianghan Plain was the main area of CO aggregation. The emission inventory showed that the anthropogenic CO emissions from the four sectors in the Jianghan Plain and its surrounding areas were 13.69 g/month/m^2 , which was about twice the average value of anthropogenic CO emissions in the Yangtze River Economic Belt, making the area to be a centralized region with high values of ground-level concentrations of CO.

The Sichuan-Chongqing region was another hotspot in the Yangtze River Economic Belt, with the Sichuan Basin as the center of dispersion outwards. The ground-level CO concentration in the Sichuan basin reached more than twice the average concentration in the Sichuan-Chongqing region. The main reason for this phenomenon is that the Sichuan basin contains the main areas of the Sichuan-Chongqing urban agglomeration. The Chengdu-Chongqing urban agglomeration has superior location conditions and can allocate resource factors and expand markets on a larger spatial scale, since it is located at the conjunctions where east meets west and north meets south. Therefore, the anthropogenic CO emissions in this region are high. The emission inventory showed that the average value of anthropogenic CO emissions in the Sichuan Basin is 11.49 g/month/m^2 , which is 67.9% higher than the average value in the Yangtze River Economic Belt. In addition, the low-level stationary vortex flow associated with the topographic features of

the basin and the barrier of the mountains around the basin are not conducive to the diffusion of CO concentrations (Chen et al., 2009), which also contributes to the formation of CO concentration areas.

The MGWR model directly reflected the differences in the action scales of the auxiliary factors in forming this spatial variation. Table 1 shows the output bandwidths and regression coefficients from the MGWR model. The bandwidth reflected the minimum search distance required for the model to converge. Smaller bandwidth indicated that the CO concentration was more spatially sensitive to the factor. The bandwidth of the output indicated that ground-level CO concentrations were sensitive to geographic location, terrain height, temperature, and precipitation with a small scale of action. In contrast, the effects of population and nighttime light intensity on ground-level CO concentrations were relatively stable at scales of 193 and 1823, indicating that population and nighttime light intensity had prominent effects at any scale. Fig. 3 (b)–(g) describes the characteristics of the spatial distribution of the individual regression coefficients calculated from the MGWR model.

The geographic location represented by the intercept determined the concentration of CO emissions. There was a high degree of overlaps of positive values and areas of high ground-level CO concentration. These regions have a high level of urbanization and high CO emissions, which have a significant positive impact on ground-level CO concentrations. The regression coefficient of the DEM showed negative values

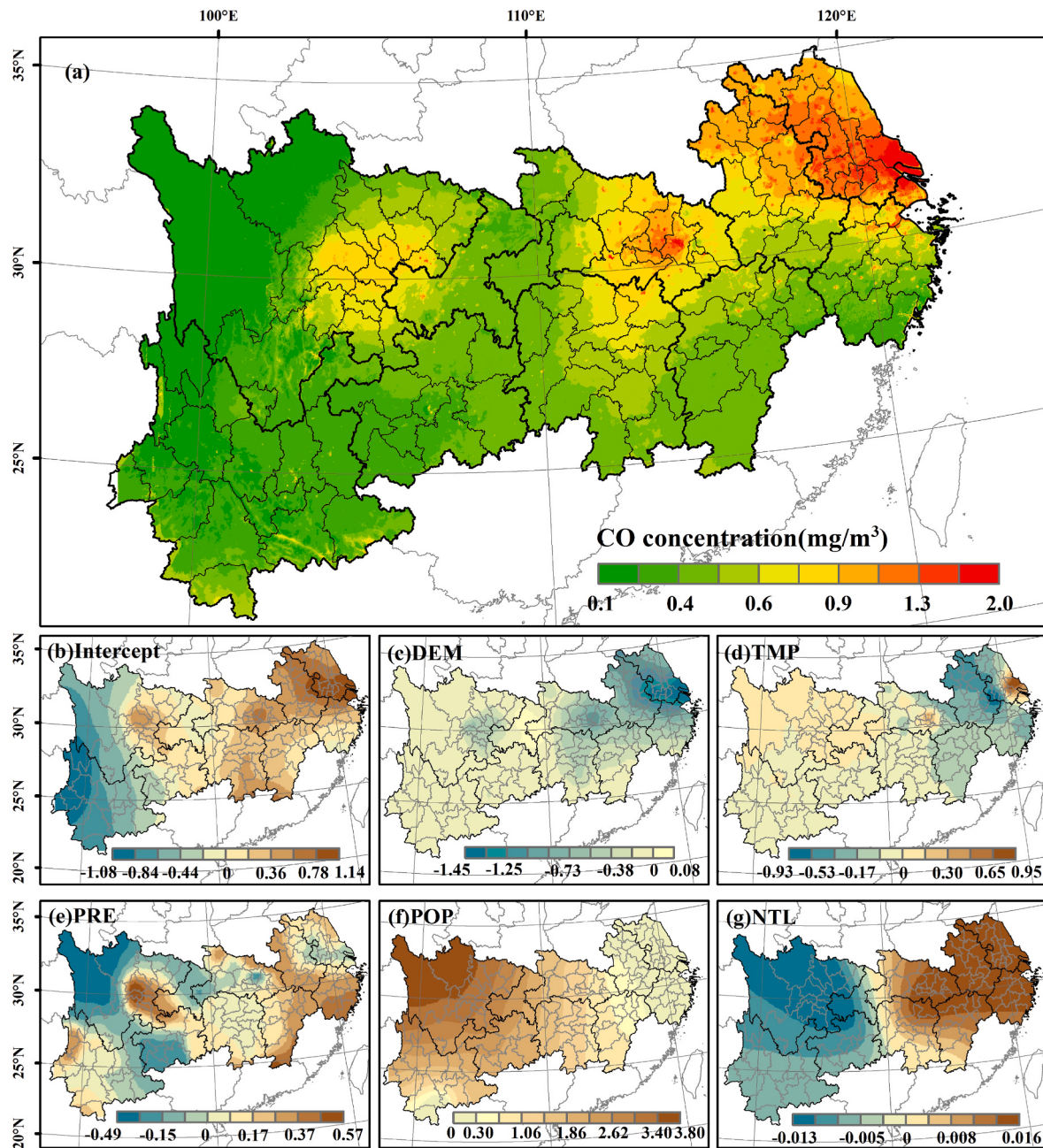


Fig. 3. Ground-level CO concentrations in 2020 (a) and the pattern of coefficients for auxiliary variables from the MGWR model (b)–(g).

throughout the Yangtze River Economic Belt region, except for central Chongqing and its surrounding areas. Chongqing has many mountainous areas with large variations in terrain, which leads to a local accumulation of elevated CO in long-range transport when it encounters topographic blockage. In contrast, the higher the terrain height and the higher the wind speed in other areas, the faster the trend of decreasing CO concentrations, forming a pattern of vertically decreasing CO concentrations.

The positive values of temperature regression coefficients were concentrated in the Sichuan and Chongqing regions, while the values were negative in the rest of the regions. This means temperature was negatively correlated with CO concentration in the majority of regions. The topography of the Sichuan and Chongqing regions is relatively closed, with mountains such as the Qinling and Daba mountain ranges blocking the entry of airflow from other regions, causing the regression coefficients in this region to exhibit opposite results from neighboring

spaces. The spatial variation in the effect of precipitation on CO concentrations is the strongest among these influencing factors, with the effect of precipitation in adjacent spaces showing two opposing trends.

The intensity of population increasing from west to east reflected the positive influence of human life and industrial emissions on the enhancement of CO concentrations (Liu et al., 2013). Due to the lack of large-scale industrial emissions, household and individual-based emissions were the main sources of CO emissions in the western, and population density had a significant positive effect on CO concentrations. While in the eastern coastal areas, population density was generally high so the spatial heterogeneity of ground-level CO concentrations was mainly influenced by other factors. The impact of nighttime light intensity decreased from east to west and shifted from a positive to a negative impact. The nighttime lighting data showed that the focus of China's economy was in the east, especially in the southeastern coastal region where the lights were dense. The positive effect of nighttime

lighting on CO concentrations was not reflected in the west where there were only a few bright spots.

Ground-level CO concentrations with a spatial resolution of $1 \text{ km} \times 1 \text{ km}$ reflected more detailed local information. Six provincial capitals were selected to compare CO concentrations in the urban core and its surrounding areas because these cities have abundant number of ground stations in the buffer zone at different distances (Fig. 4). This data reflected urban-rural concentration differences that cannot be expressed in the data with course spatial resolution. Based on land use and the location of each city center, buffer zones of 3 km, 5 km, 8 km, 12 km, and 17 km were established around the city center and the averages of CO concentrations in each buffer zone was calculated. There was a gradient decrease in CO concentrations from the main urban areas to the background areas and the CO concentrations observed at the sites showed a similar trend.

The CO concentration over different land uses is shown in Fig. 5. The highest CO occurred in urban areas. The relatively higher CO concentrations in urban areas were mainly determined by CO emissions. The heavy traffic in urban areas emitted more CO since vehicle exhaust is a CO source. Therefore, the hotspots of CO concentration had a high overlap in geographical distribution with cities which are populated and industrially developed. The average of ground-level CO concentration in farmland areas was 0.65 mg/m^3 , which was significantly higher than that in other areas, including 0.41 mg/m^3 in woodland, 0.28 mg/m^3 in grassland, and 0.22 mg/m^3 in unused land. About 42% of the total CO emissions come from industrial and biomass combustion activities (Pommier et al., 2013). In addition, farmlands are in the transition zone from urban areas to woodlands, and these transition zones are open, flat and geographically close to urban areas, thus enhancing the diffuse transport of CO pollutants. The heterogeneity of urban and rural CO concentrations indicated that the spatial downscaling approach based on the MGWR model was effective in adding textural information.

3.3. Seasonal variation of the ground-level CO concentrations in the Yangtze River Economic Belt

In this study, 12 months of ground-level CO concentrations with the spatial resolution of $1 \text{ km} \times 1 \text{ km}$ in the Yangtze River Economic Belt in 2020 was constructed to explore seasonal variation (see Fig.B2 in SI.B). Monthly mean ground-level CO concentrations in the Yangtze River

Economic Belt ranged from 0.30 to 0.81 mg/m^3 and an average of 0.49 mg/m^3 (Table 2).

Ground-level CO concentrations in 2020 showed a decreasing trend in the first half of the year and then increasing in the second half. CO pollution was lowest in summer. The small standard deviations in July and August indicated that ground-level CO concentrations did not vary significantly across the Yangtze River Economic Belt. The averages of CO concentrations were low in spring and autumn, but the high values in hot spots were still relatively significant. Compared to summer, the standard deviation was elevated and the extent of CO pollution was expanded. The peaks of ground-level CO concentrations occurred in the colder months, with the highest standard deviation and the widest distribution of pollution. Ground-level CO concentrations increased significantly in October and reached a maximum value in December. CO pollution was severe in January, February, November and December, with areas of high values concentrated in patches.

Lower CO concentrations were concentrated in summer mainly due to the effect of rainfall on the wet deposition of gaseous pollutants. Precipitation has a flushing, diluting, diffusing and removing effect on atmospheric pollutants (Yang et al., 2019). The increased strength of the southwest monsoon in summer brought more rainfall, and the CO concentration decreased significantly through the wet deposition effect of rainfall. In addition, the high temperature and low pressure in summer will intensify the vertical movement of the atmosphere and strengthen turbulence (Feng, 2022), which accelerates the diffusion and dilution of atmospheric pollutants and the rapid dissipation of atmospheric pollutants. Moreover, atmospheric chemical reactions are active and the concentration of hydroxyl groups is high in summer, so that carbon monoxide is easily oxidized to form carbon dioxide and thus removed from the atmosphere.

CO concentrations started to rise in October. The increase in CO concentrations during this period comes mainly from biomass burning, with October as the peak month for agricultural straw burning (Li et al., 2015). The highest CO concentrations reached in December. The result was consistent with the study by Feng et al. (2020), which showed that the significant increase in CO emissions in December was due to a peak in CO emissions from residential heating caused by the cold winter. According to the National Bureau of Statistics, power generation in December was 5.38 billion kilowatts in 2020, 51% above the annual average (3.56 billion kilowatts). In addition, cold air currents with

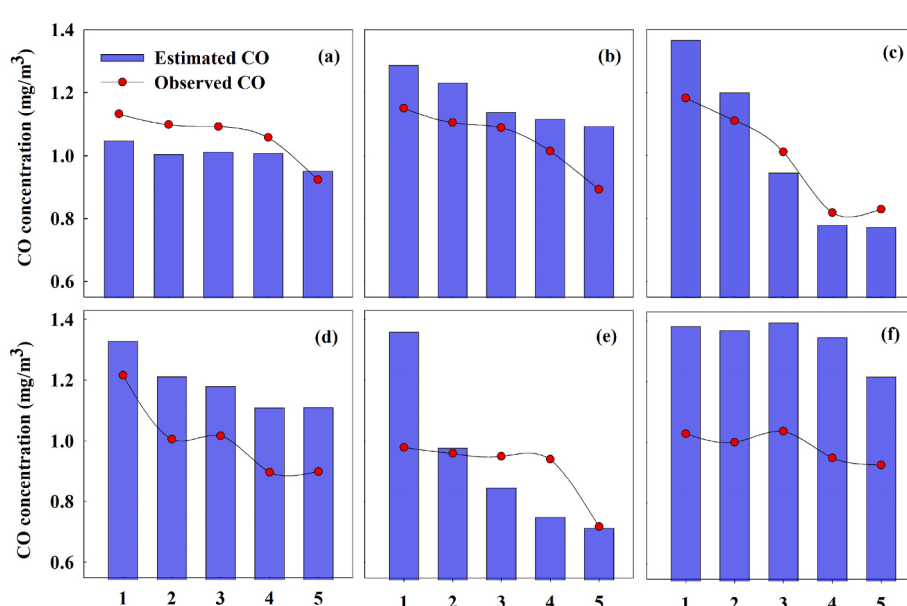


Fig. 4. Estimated and observed ground-level CO concentrations along the transect from urban to its surrounding areas at (a) Changsha (b) Chengdu (c) Chongqing (d) Hangzhou (e) Nanchang (f) Wuhan (1–5 corresponds to buffer zones of 3 km, 5 km, 8 km, 12 km and 17 km from the city center).

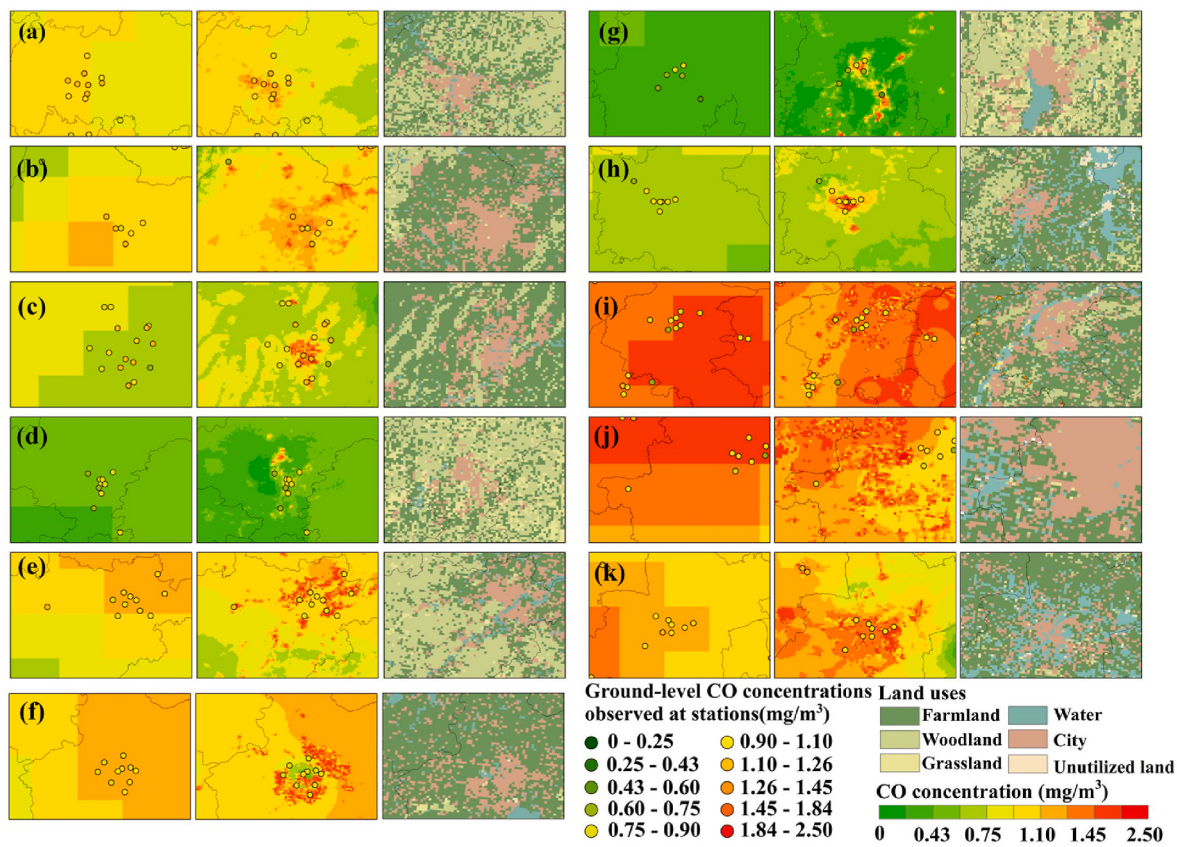


Fig. 5. Comparison of CO concentrations in different land use types of provincial capital cities (a) Changsha (b) Chengdu (c) Chongqing (d) Guiyang (e) Hangzhou (f) Hefei (g) Kunming (h) Nanchang (i) Nanjing (j) Shanghai (k) Wuhan, column 1 of each set of graphs represents CO concentrations with the spatial resolution of $0.25^\circ \times 0.25^\circ$, column 2 of each set of graphs represents CO concentrations with the spatial resolution of $1 \text{ km} \times 1 \text{ km}$, column 3 of each set of graphs represents land uses.

Table 2
Statistics of monthly CO concentrations in the Yangtze River Economic Belt.

Month	Jan.	Feb.	Mar.	Apr.	May	Jun.	Jul.	Aug.	Sep.	Oct.	Nov.	Dec.
Average(mg/m^3)	0.59	0.66	0.55	0.50	0.42	0.30	0.34	0.35	0.39	0.48	0.61	0.81
Standard deviation(mg/m^3)	0.32	0.39	0.31	0.32	0.30	0.26	0.21	0.17	0.24	0.28	0.37	0.50

pollutants from the northwest pushed towards the southeast in December, which led to the increase in CO concentrations (Zhu et al., 2016). Moreover, temperatures are cooler and air pressure is higher in winter. Under the control of high pressure systems, the air over a wide area makes a sinking movement and tends to form an inverse thermosphere. This high pressure control is accompanied by low temperatures to form a stable atmospheric nodule, both of which are not conducive to pollutant dispersion.

3.4. The uncertainty analysis of the proposed method in estimating ground-level CO concentrations

Besides of the method proposed in this study, some other methods have also been used to obtain high-resolution spatial distributions of ground-level atmospheric pollutant concentrations by inversion based on machine learning and multi-source data fusion (Brokamp et al., 2018; Zhan et al., 2018; You et al., 2019). However, the method requires coupling a large number of ground station monitoring data to train the dataset. Compared with that, the monitoring data from the ground stations in this study were not involved in constructing model and were only used as validation data. To a certain extent, it can effectively compensate for the lack of spatially extended information caused by sparse monitoring data on the ground. In addition, it has simple

parameters and is less likely to fall into the problem of local optimal tuning range.

The CO columns were often used as a proxy to ground-level concentrations. Fig. 6 (a) shows the comparison between MOPITT CO columns and ground observations. As a whole, the spatial distribution with high in the east and low in the west was consistent with that in ground observations. However, if CO columns are used instead of ground-level data, the effect of vertical transport bias on CO inversion concentrations needs to be considered. Previous studies have confirmed that the limited vertical resolution of the satellite means that the retrieved lower tropospheric CO is influenced by the free tropospheric CO (Jiang et al., 2013; Buchholz et al., 2017; Hedelius et al., 2021). Fig. 6 (b) compares the CO columns to the ground-level concentrations derived in this study. Although R of 0.83 is high, the values for columns do not agree numerically with those derived by combining atmospheric chemistry models. The RMSE and the mean absolute error (MAE) are large. In addition, the spatial heterogeneity of the CO columns is low and does not convey the difference in CO concentrations between neighboring regions. Therefore, this study could obtain more accurate results by deriving columns to ground-level concentrations first and then performing spatial downscaling.

When performing spatial downscaling, this study has taken account of the synergistic effects of various factors on ground-level CO

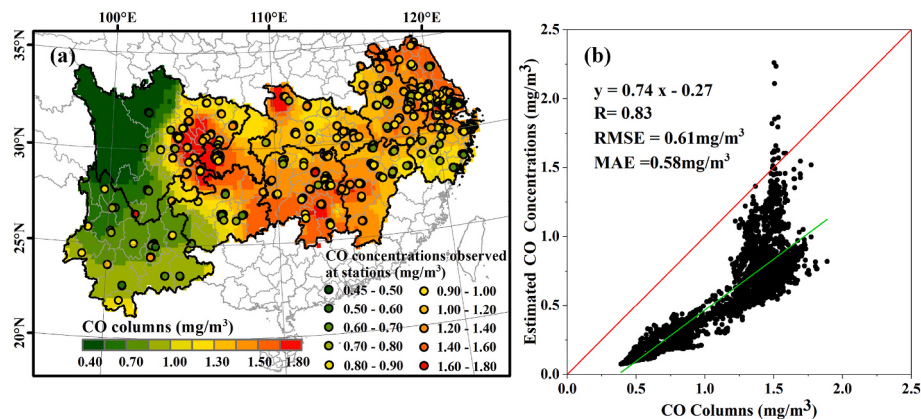


Fig. 6. (a) Spatial distribution of CO columns from MOPITT, (b) scatterplot between the ground-level CO concentrations simulated by CAM-CHEM and CO columns.

concentrations. Giorgi and Meleux (2007) found emission sources and meteorological factors jointly determine the concentration of atmospheric pollutants. The nighttime lighting data and population data selected for this study denoted the influence of human activities on ground-level CO concentrations, which is the most significant influence on CO emission differences. The precipitation and temperature represented the influence of meteorological influences. The regression results from this study showed that the population factor had the greatest influence on ground-level CO concentrations. Compared with the global adjusted R^2 of 0.22 for the regression results of selecting only demographic factors, the global adjusted R^2 of 0.99 for the regression of auxiliary factors considered in this study was significantly higher, which can effectively represent the synergistic effect of influencing factors on ground-level CO concentrations.

Certainly, more variables were used in downscaling CO concentrations, more uncertainties were induced. The precision of MOPITT CO columns have an impact on the estimation results on ground-level CO concentrations through error transfer. Deeter et al. (2007) showed that the correlation coefficient was 0.93 between the MOPITT CO monthly-scale product and the validation data, with a bias of 0.3×10^{17} molecules/cm², when compared to in-situ measurements at the National Oceanic and Atmospheric Administration (NOAA) tropospheric CO validation site. The inversion of the monthly-scale MOPITT CO product arise from data smoothing errors, errors in the inversion model parameters, and instrument noise errors. The uncertainty caused by the vertical altitude range of CO monitored by the MOPITT sensor from near the surface to the top of the troposphere is about 8.4% (Fu et al., 2016). In addition, there are local differences between satellite and ground-based CO observations. The former is mainly sensitive to free tropospheric CO, which is strongly influenced by long-range transport, while the latter is mainly sensitive to local emissions. Tang et al. (2022) demonstrated that the trends in MOPITT and ground-level CO concentrations in eastern China are different, and these differences affect the accuracy of the satellite-based ground-based CO concentrations derived in this study.

The uncertainty in fitting ground-level CO concentrations using atmospheric chemistry model profiles combined with satellite observations mainly comes from the influence of adverse meteorological conditions on the profile fitting process. The CO profile along the vertical direction of the atmosphere is influenced by seasonal boundary layer height variations. The planetary boundary layer height determines the dispersion characteristics of pollutants in the vertical direction of the atmosphere, which has an important influence on the ground-level pollutant concentrations (Huang et al., 2021).

The uncertainty of downscaling algorithms based on MGWR model is mainly influenced by the environmental characteristics, the quality and availability of auxiliary data products and errors in the conversion process. Due to the relative complexity of land cover types and

topographic features on land surfaces, some studies have shown that the ‘relational scale invariance’ assumption can be successfully applied to topographically homogeneous surfaces and areas with homogeneous land cover. However, there may be some limitations in its applicability to landscapes with heterogeneous surfaces (Mukherjee et al., 2014; Hutengs and Vohland, 2016). The local regression models constructed differ due to different geographical locations and topographic features in different regions, but overall have a similar regression form. In addition, smoothing effects may occur in the spatial aggregation of the auxiliary data. In this process, the values of the auxiliary data are replaced by the average of the surrounding pixels, which may produce a smoothing effect and result in loss of detailed information (Xu et al., 2015). Therefore spatial sharpening of ground-level CO data using stepwise downscaling in future studies would be expected to achieve higher spatial downscaling accuracy.

4. Conclusion

A spatial downscaling method was proposed to obtain high-resolution CO concentrations at ground level, from MOPITT CO columns and the chemical transport model CAM-CHEM. The method first converted MOPITT CO columns into the ground level concentrations with coarse resolution, considering the CO variations along atmospheric heights from CAM-CHEM; then a non-smooth relationship between CO concentration and other environmental factors was established to convert the coarse resolution to fine resolution, based on a MGWR model. The high resolution CO concentrations clearly captured the detailed texture within each image element of the original ground-level CO image and guaranteed the accuracy of the ground-level CO concentration downscaling results.

There were strong spatial and seasonal variations in ground-level CO concentrations in the Yangtze River Economic Belt. Spatially, the hot-spots of CO concentrations were focused in the northern Yangtze River Delta, the middle of Hubei Province, the northern part of Hunan Province, the Sichuan and Chongqing regions. There was a high overlap between the spatial distribution of high CO concentration areas and urban areas. Temporally, peak ground-level CO concentrations occurred in colder months, with the most serious CO pollution occurring in January, February, November and December. CO pollution was lightest in summer.

Funding statement

This study is supported by the Basic Research Program of Jiangsu Province (No.: BK20211156), Jiangsu Province Science and Technology Innovation Program of Carbon Peaking and Carbon Neutrality (BK20220037), open Fund of Key Laboratory of Urban Land Resources Monitoring and Simulation, Ministry of Natural Resources (No.: KF-

2021-06-028), and Analysis of the Spatial Pattern of Land Use of Carbon Emissions in the Yangtze River Delta Region (NO.: 2023200243).

CRediT authorship contribution statement

Jiaqi Dong: Conceptualization, Methodology, Validation, Investigation, Data curation, Writing – original draft, Writing – review & editing. **Xiuying Zhang:** Conceptualization, Methodology, Writing – review & editing, Supervision, Project administration, Funding acquisition. **Nan Zhan:** Resources, Visualization.

Declaration of competing interest

The authors declare that they have no known competing financial interests or personal relationships that could have appeared to influence the work reported in this paper.

Data availability

Data will be made available on request.

Acknowledgment

We acknowledged the use of MOPITT CO columns (<https://asdc.larc.nasa.gov/data/MOPITT/MOP02J.008/>), CO profile from CAM-CHEM (<https://www.acm.ucar.edu/cam-chem>), in-situ measurements of CO concentrations (<http://www.cnemc.cn/>), monthly temperature and precipitation data (<https://data.tpdc.ac.cn/>), global nighttime lighting data (<http://www.nasa.gov/NPP>), gridded population data (<https://sedac.ciesin.columbia.edu/data/set>), digital topographic elevation data (<https://earthexplorer.usgs.gov/>) and the land use data (<http://www.resdc.cn/>).

Appendix A. Supplementary data

Supplementary data to this article can be found online at <https://doi.org/10.1016/j.atmosenv.2023.120018>.

References

- Alahmadi, S., Al-Ahmadi, K., Almeshari, M., 2019. Spatial variation in the association between NO₂ concentrations and shipping emissions in the Red Sea. *Sci. Total Environ.* 676, 131–143. <https://doi.org/10.1016/j.scitotenv.2019.04.161>.
- Allen, D.R., Stanford, J.L., Lopez-Valverde, M.A., Nakamura, N., Lary, D.J., Douglass, A.R., Cerniglia, M.C., Remedios, J.J., Taylor, F.W., 1999. Observations of middle atmosphere CO from the UARS ISAMS during the early northern winter 1991/92. *J. Atmos. Sci.* 56 (4), 563–583. [https://doi.org/10.1175/1520-0469\(1999\)056<563:OOMACF>2.0.CO;2](https://doi.org/10.1175/1520-0469(1999)056<563:OOMACF>2.0.CO;2).
- Brokamp, C., Jandarov, R., Hossain, M., Ryan, P., 2018. Predicting daily urban fine particulate matter concentrations using a random forest model. *Environ. Sci. Technol.* 52 (7), 4173–4179. <https://doi.org/10.1021/acs.est.7b05381>.
- Buchholz, R.R., Deeter, M.N., Worden, H.M., Gille, J., Edwards, D.P., Hannigan, J.W., Jones, N.B., Paton-Walsh, C., Griffith, D.W.T., Smale, D., Robinson, J., Strong, K., Conway, S., Sussmann, R., Hase, F., Blumenstock, T., Mahieu, E., Langerock, B., 2017. Validation of MOPITT carbon monoxide using ground-based Fourier transform infrared spectrometer data from NDACC. *Atmos. Meas. Tech.* 10, 1927–1956. <https://doi.org/10.5194/amt-10-1927-2017>.
- Chen, J., He, W., Chen, H., 2015. Spatial and temporal distribution characteristics of tropospheric CO over Asia using MOPITT data. *Climatic Environ. Res.* 20 (6), 635–644. <https://doi.org/10.3878/j.issn.1006-9585.2015.15085>.
- Chen, D., Wang, Y., McElroy, M.B., He, K., Yantosca, R.M., Le Sager, P., 2009. Regional CO pollution and export in China simulated by the high-resolution nested-grid GEOS-Chem model. *Atmos. Chem. Phys.* 9 (11), 3825–3839. <https://doi.org/10.5194/acp-9-3825-2009>.
- Chen, P., Zhang, Q., Quan, J., Gao, Y., Zhao, D., Meng, J., 2012. Temporal and spatial distribution of atmospheric pollutants by aircraft sounding in 3500m altitude of Beijing area. *China Environ. Sci.* 32 (10), 1729–1735. <https://doi.org/10.3969/j.issn.1000-6923.2012.10.001>.
- Cheng, X., Wu, W., Xia, L., Luo, R., Shen, Z., 2017. Automatic extraction method for impervious surface area by integrating nighttime light data and Landsat TM images. *J. Geo. Inf. Sci.* 19 (10), 1364–1374. <https://doi.org/10.3724/SP.J.1047.2017.01364>.
- Deeter, M.N., Edwards, D.P., Gille, J.C., Drummond, J.R., 2007. Sensitivity of MOPITT observations to carbon monoxide in the lower troposphere. *J. Geophys. Res. Atmos.* 112 (D24) <https://doi.org/10.1029/2007jd008929>.
- Feng, S.Z., Jiang, F., Wu, Z., Wang, H., Ju, W., Wang, H., 2020. CO emissions inferred from surface CO observations over China in December 2013 and 2017. *J. Geophys. Res. Atmos.* 125 (7) <https://doi.org/10.1029/2019JD031808>.
- Feng, S., 2022. Influence of meteorological factors on air pollutants and construction of prediction model. *Environ. Sci. Manag.* 47 (8), 61–65. <https://doi.org/10.3969/j.issn.1673-1212.2022.08.014>.
- Fotheringham, A.S., Yang, W.B., Kang, W., 2017. Multiscale geographically weighted regression (MGWR). *Ann. Assoc. Am. Geogr.* 107 (6), 1247–1265. <https://doi.org/10.1080/24694452.2017.1352480>.
- Fu, D.J., Bowman, K.W., Worden, H.M., Natraj, V., Worden, J.R., Yu, S.S., Veefkind, P., Aben, I., Landgraf, J., Strow, L., Han, Y., 2016. High-resolution tropospheric carbon monoxide profiles retrieved from CrIS and TROPOMI. *Atmos. Meas. Tech.* 9 (6), 2567–2579. <https://doi.org/10.5194/amt-9-2567-2016>.
- Giorgi, F., Meleux, F., 2007. Modelling the regional effects of climate change on air quality. *Compt. Rendus Geosci.* 339 (11), 721–733. <https://doi.org/10.1016/j.crte.2007.08.006>.
- Glaser, K., Vogt, U., Baumback, G., Volz-Thomas, A., Geiss, H., 2003. Vertical profiles of O₃, NO₂, NOx, VOC, and meteorological parameters during the Berlin Ozone Experiment (BERLIOZ) campaign. *J. Geophys. Res. Atmos.* 108 (D4) <https://doi.org/10.1029/2002jd002475>.
- Goodchild, M.F., 2013. Prospects for a space-time GIS. *Ann. Assoc. Am. Geogr.* 103 (5), 1072–1077. <https://doi.org/10.1080/0045608.2013.792175>.
- Gu, J.B., Chen, L.F., Yu, C., Li, S.S., Tao, J.H., Fan, M., Xiong, X.Z., Wang, Z.F., Shang, H.Z., Su, L., 2017. Ground-level NO₂ concentrations over China inferred from the satellite OMI and CMAQ model simulations. *Rem. Sens.* 9 (6) <https://doi.org/10.3390/rs9060519>.
- Hedelius, J.K., Toon, G.C., Buchholz, R.R., Iraci, L.T., Podolske, J.R., Roehl, C.M., Wennberg, P.O., Worden, H.M., Wunch, D., 2021. Regional and urban column CO trends and anomalies as observed by MOPITT over 16 years. *J. Geophys. Res. Atmos.* 126, e2020JD033967 <https://doi.org/10.1029/2020jd033967>.
- Hu, J.L., Chen, J.J., Ying, Q., Zhang, H.L., 2016. One-year simulation of ozone and particulate matter in China using WRF/CMAQ modeling system. *Atmos. Chem. Phys.* 16 (16), 10333–10350. <https://doi.org/10.5194/acp-16-10333-2016>.
- Hu, M.M., Wang, Y.F., Wang, S., Jiao, M.Y., Huang, G.H., Xia, B.C., 2021. Spatial-temporal heterogeneity of air pollution and its relationship with meteorological factors in the Pearl River Delta, China. *Atmos. Environ.* 254 <https://doi.org/10.1016/j.atmosenv.2021.118415>.
- Hu, Z.K., Li, A., Xie, P.H., Wu, F.C., Xu, J., Yang, L., Huang, Y.Y., 2019. Study on concentration distribution reconstruction method of pollution gas column. *Spectrosc. Spectr. Anal.* 39 (9), 2670–2676. [https://doi.org/10.3964/j.issn.1000-0593\(2019\)09-2670-07](https://doi.org/10.3964/j.issn.1000-0593(2019)09-2670-07).
- Huang, Y.X., Guo, B., Sun, H.X., Liu, H.J., Chen, S.X., 2021. Relative importance of meteorological variables on air quality and role of boundary layer height. *Atmos. Environ.* 267 <https://doi.org/10.1016/j.atmosenv.2021.118737>.
- Hutengs, C., Vohland, M., 2016. Downscaling land surface temperatures at regional scales with random forest regression. *Remote Sens. Environ.* 178, 127–141. <https://doi.org/10.1016/j.rse.2016.03.006>.
- Jiang, Z., Jones, D.B.A., Worden, H.M., Deeter, M.N., Henze, D.K., Worden, J., Bowman, K.W., Breninkmeijer, C.A.M., Schuck, T.J., 2013. Impact of model errors in convective transport on CO source estimates inferred from MOPITT CO retrievals. *J. Geophys. Res. Atmos.* 118, 2073–2083. <https://doi.org/10.1029/jgrd.50216>.
- Kollonige, D.E., Thompson, A.M., Josipovic, M., Tzortziou, M., Beukes, J.P., Burger, R., Martins, D.K., Van, P.G., Vakkari, V., Laakso, L., 2018. OMI Satellite and ground-based Pandora observations and their application to surface NO₂ estimations at terrestrial and marine sites. *J. Geophys. Res. Atmos.* 123 (2), 1441–1459. <https://doi.org/10.1002/2017jd026518>.
- Lamsal, L.N., Martin, R.V., Van, D.A., Steinbacher, M., Celarier, E.A., Bucsela, E., Dunleavy, E.J., Pinto, J.P., 2008. Ground-level nitrogen dioxide concentrations inferred from the satellite-borne Ozone Monitoring Instrument. *J. Geophys. Res. Atmos.* 113 (D16) <https://doi.org/10.1029/2007jd009235>.
- Li, J., Song, Y., Li, M., Huang, X., 2015. Estimating air pollutants emissions from open burning of crop residues in Jianghan Plain. *Acta Sci. Nauralium Univ. Pekin.* 51 (4), 647–656. <https://doi.org/10.13209/j.0479-8023.2015.088>.
- Li, J., Zhang, X., 2015. Downscaling method of TRMM satellite precipitation data. *Sci. Geogr. Sin.* 35 (9), 1164–1169. <https://doi.org/10.13249/j.cnki.sgs.2015.09.013>.
- Li, M., Zhang, Q., Kurokawa, J., Woo, J.H., He, K.B., Lu, Z.F., Ohara, T., Song, Y., Streets, D.G., Carmichael, G.R., Cheng, Y.F., Hong, C.P., Huo, H., Jiang, X.J., Kang, S.C., Liu, F., Su, H., Zheng, B., 2017. MIX: a mosaic Asian anthropogenic emission inventory under the international collaboration framework of the MICS-Asia and HTAP. *Atmos. Chem. Phys.* 17 (2), 935–963. <https://doi.org/10.5194/acp-17-935-2017>.
- Liu, C., Bai, W.G., Zhang, P., Sun, Y.W., Si, F.Q., 2013. The inverse method of carbon monoxide from satellite measurement and the result analysis. *Acta Phys. Sin.* 62 (3) <https://doi.org/10.7498/aps.62.030704>.
- Liu, D.R., Di, B.F., Luo, Y.Z., Deng, X.F., Zhang, H.Y., Yang, F.M., Grieneisen, M.L., Zhan, Y., 2019. Estimating ground-level CO concentrations across China based on the national monitoring network and MOPITT: potentially overlooked CO hotspots in the Tibetan Plateau. *Atmos. Chem. Phys.* 19 (19), 12413–12430. <https://doi.org/10.5194/acp-19-12413-2019>.
- Li, Y., Quan, Q., Zhu, J., Wang, F., 2018. Green technology innovation, industrial agglomeration and ecological efficiency - a case study of urban agglomerations on Yangtze River Economic belt. *Resour. Environ. Yangtze Basin* 27 (11), 2395–2406.

- Lu, Y.L., Jiang, H., Huang, J., Xu, L., 2014. Simulation of annual average SO₂ concentration of the prefecture-level cities in China based on GWR mode. *Ecol. Environ. Sci.* 23 (8), 1305–1310. <https://doi.org/10.16258/j.cnki.1674-5906.2014.08.011>.
- Ma, B., Jia, L., Yu, Y., Wang, H., Chen, J., Zhong, S., Zhu, J., 2021. Geoscience and carbon neutralization: Current status and development direction. *Chin. Geol.* 48 (2), 347–358.
- Mukherjee, S., Joshi, P.K., Garg, R.D., 2014. A comparison of different regression models for downscaling Landsat and MODIS land surface temperature images over heterogeneous landscape. *Adv. Space Res.* 54 (4), 655–669. <https://doi.org/10.1016/j.asr.2014.04.013>.
- Oshan, T.M., Li, Z.Q., Kang, W., Wolf, L.J., Fotheringham, A.S., 2019. MGWR: a Python implementation of multiscale geographically weighted regression for investigating process spatial heterogeneity and scale. *ISPRS Int. J. Geo-Inf.* 8 (6) <https://doi.org/10.3390/ijgi8060269>.
- Peng, S.Z., Ding, Y.X., Liu, W.Z., Li, Z., 2019. 1 km monthly temperature and precipitation dataset for China from 1901 to 2017. *Earth Syst. Sci. Data* 11 (4), 1931–1946. <https://doi.org/10.5194/essd-11-1931-2019>.
- Pommier, M., McLinden, C.A., Deeter, M., 2013. Relative changes in CO emissions over megacities based on observations from space. *Geophys. Res. Lett.* 40 (14), 3766–3771. <https://doi.org/10.1002/grl.50704>.
- Smith, M.W., Shertz, S.R., Delen, N., 1999. Remote sensing of atmospheric carbon monoxide with the MOPITT airborne test radiometer (MATR)[C] optical spectroscopic techniques and instrumentation for atmospheric and space Research III. *Int. Soc. Opt. Photo.* 3756, 475–485. <https://doi.org/10.1117/12.366406>.
- Sørensen, J.H., 1998. Sensitivity of the DERMA long-range Gaussian dispersion model to meteorological input and diffusion parameters. *Atmos. Environ.* 32, 4195–4206. [https://doi.org/10.1016/S1352-2310\(98\)00178-2](https://doi.org/10.1016/S1352-2310(98)00178-2).
- Sutton, O.G., 1947. The problem of diffusion in the lower atmosphere. *Q. J. Roy. Meteorol. Soc.* 73, 257e281.
- Tang, Z., Chen, J., Jiang, Z., 2022. Discrepancy in assimilated atmospheric CO over East Asia in 2015–2020 by assimilating satellite and surface CO measurements. *Atmos. Chem. Phys.* 22, 7815–7826. <https://doi.org/10.5194/acp-22-7815-2022>.
- Wang, R., Gao, W.J., Peng, W.C.Y., 2021. Spatial downscaling method for air temperature through the correlation between land use/land cover and microclimate: a case study of the Greater Tokyo Area. *Urban Clim.* 40 <https://doi.org/10.1016/j.ulcim.2021.101003>.
- Wang, S., Ackermann, R., Stutz, J., 2006. Vertical profiles of O₃ and NO_x chemistry in the polluted nocturnal boundary layer in Phoenix, AZ: I. Field observations by long-path DOAS. *Atmos. Chem. Phys.* 6, 2671–2693. <https://doi.org/10.5194/acp-6-2671-2006>.
- Wang, T., Cheung, T.F., Li, Y.S., Yu, X.M., Blake, D.R., 2002. Emission characteristics of CO, NO_x, SO₂ and indications of biomass burning observed at a rural site in eastern China. *J. Geophys. Res. Atmos.* 107 (D12) <https://doi.org/10.1029/2001jd000724>.
- Wang, Y., Xie, D., Li, Y., 2014. Downscaling remotely sensed land surface temperature over urban areas using trend surface of spectral index. *J. Remote Sens.* 18 (6), 1169–1181. <https://doi.org/10.11834/jrs.20144115>.
- Wei, Z., Meng, Y., Zhang, W., Peng, J., Meng, L.K., 2019. Downscaling SMAP soil moisture estimation with gradient boosting decision tree regression over the Tibetan Plateau. *Remote Sens. Environ.* 225, 30–44. <https://doi.org/10.1016/j.rse.2019.02.022>.
- Xu, L., Chen, F., Chen, F., Chen, W., Yu, H., Huang, X., Zeng, Y., Li, X., Hong, S., Feng, Y., Zhong, X., 2014. Spatial and temporal variation of near-ground CO concentration in the eight economic regions in China in may and july, 2013. *Acta Sci. Circumstantiae* 34 (8), 1934–1941. <https://doi.org/10.13671/j.hjkxxb.2014.0642>.
- Xu, S.G., Wu, C.Y., Wang, L., Gonsamo, A., Shen, Y., Niu, Z., 2015. A new satellite-based monthly precipitation downscaling algorithm with non-stationary relationship between precipitation and land surface characteristics. *Remote Sens. Environ.* 162, 119–140. <https://doi.org/10.1016/j.rse.2015.02.024>.
- Yan, H.H., Li, X.J., Wang, W.H., Zhang, X.Y., Chen, L.F., Han, D., Yu, C., Gao, L., 2017. Comparison of SO₂ column retrievals from BRD and DOAS algorithms. *Sci. China Earth Sci.* 60 (9), 1694–1706. <https://doi.org/10.1007/s11430-016-9057-6>.
- Yang, G.P., Ren, C.Y., Lu, X.L., Liu, C.Y., Ding, H.B., 2011. Distribution, flux, and photoproduction of carbon monoxide in the East China Sea and Yellow Sea in spring. *J. Geophys. Res. C Oceans* 116. <https://doi.org/10.1029/2010jc006300>.
- Yang, Q., Gao, Y., Chen, G., 2019. Influence analysis of the precipitation on atmospheric pollutant concentration in Chongqing. *Meteorol. Environ. Sci.* 42 (2), 68–73. <https://doi.org/10.16765/j.cnki.1673-7148.2019.02.010>.
- Yang, S., Zhang, Y., Geng, Y., 2022. Examining the changes in carbon emissions of the transportation sector in the Yangtze River Economic Belt - a LMDI and Theil index-based approach. *China Environ. Sci.* 1–23. <https://doi.org/10.19674/j.cnki.issn1000-6923.20220530.002>.
- You, J.W., Zou, B., Zhao, X.G., Xu, S., He, R., 2019. Estimating ground-level NO₂ concentrations across mainland China using random forests regression modeling. *China Environ. Sci.* 39 (3), 969–979.
- Zhan, Y., Luo, Y.Z., Deng, X.F., Zhang, K.S., Zhang, M.H., Grieneisen, M.L., Di, B.F., 2018. Satellite-based estimates of daily NO₂ exposure in China using hybrid random forest and spatiotemporal kriging model. *Environ. Sci. Technol.* 52 (7), 4180–4189.
- Zhang, J., Wang, M., 2001. Numerical simulations on the change of atmospheric carbon monoxide. *Atmos. Sci. (6)*, 847–855. <https://doi.org/10.3878/j.issn.1006-9895.2001.06.12>.
- Zhang, X.Y., Lu, X.H., Liu, L., Chen, D.M., Zhang, X.M., Liu, X.J., Zhang, Y., 2017. Dry deposition of NO₂ over China inferred from OMI columnar NO₂ and atmospheric chemistry transport model. *Atmos. Environ.* 169, 238–249. <https://doi.org/10.1016/j.atmosenv.2017.09.017>.
- Zhang, X.Y., Zhao, L.M., Cheng, M.M., Chen, D.M., 2020. Estimating ground-level ozone concentrations in eastern China using satellite-based precursors. *IEEE Trans. Geosci. Rem. Sens.* 58 (7), 4754–4763. <https://doi.org/10.1109/tgrs.2020.29966780>.
- Zheng, B., Chevallier, F., Ciais, P., Yin, Y., Deeter, M.N., Worden, H.M., Wang, Y.L., Zhang, Q., He, K.B., 2018. Rapid decline in carbon monoxide emissions and export from East Asia between years 2005 and 2016. *Environ. Res. Lett.* 13 (4) <https://doi.org/10.1088/1748-9326/aab2b3>.
- Zheng, Y., He, Y., Wang, X., Gao, Y., 2020. Application review and prospect of nighttime light remote sensing data. *Remote Sens. Inf.* 35 (3), 1–14. <https://doi.org/10.18306/dlkxjz.2019.02.005>.
- Zhu, S., Zhou, M., Qiao, L., Li, L., Lou, S., Yan, R., Wang, H., Tao, S., Chen, C., 2016. Impact of the air mass trajectories on PM_{2.5} concentrations and distribution in the Yangtze River Delta in December 2015. *Acta Sci. Circumstantiae* 36 (12), 4285–4294. <https://doi.org/10.13671/j.hjkxxb.2016.0166>.
- Zhu, X., Song, X., Leng, P., Hu, R., 2021. Spatial downscaling of land surface temperature with the multi-scale geographically weighted regression. *J. Remote Sens.* 25 (8), 1749–1766. <https://doi.org/10.11834/jrs.20211202>.